JOURNAL OF GEOPHYSICAL RESEARCH, VOL. 112, B11307, doi:10.1029/2006JB004700, 2007

Teleseismic *P* wave imaging of the 26 December 2004 Sumatra-Andaman and 28 March 2005 Sumatra earthquake ruptures using the Hi-net array

Miaki Ishii,[1] Peter M. Shearer,[2] Heidi Houston,[3] and John E. Vidale[3]

Received 10 August 2006; revised 6 July 2007; accepted 17 August 2007; published 24 November 2007.

[1] Seismograms from a dense, high-quality seismic network in Japan are used to investigate the characteristics of the 26 December 2004 Sumatra-Andaman and the 28 March 2005 Sumatran earthquakes. The onset of the *P* waveforms are aligned through cross correlation, and a simple concept of back-projecting seismic energy to a grid of potential source locations is applied. The waveform alignment removes the effects due to lateral variations in wave speed between the hypocenter and each station. To better approximate the effects of three-dimensional heterogeneity for paths originating from grid points away from the hypocenter, cross-correlation results of the *P* waveforms from aftershocks are introduced. This additional information leads to improved resolution of smaller-scale features near many of the aftershocks by reducing wavefront distortion. The back-projection analysis provides a quick assessment of the spatiotemporal extent and variability of relative high-frequency energy release, which can be translated into an estimate of the moment magnitude, as well as an unparalleled view of high-frequency rupture propagation. The results are, in general, consistent with those obtained from more involved source inversion methods. The 2004 Sumatra-Andaman earthquake released most energy in a region northwest of the Sumatra island and the rupture extended to the northern Andaman islands, about 1300 km from the epicenter. This northern portion of the rupture radiated a considerable amount of energy, but there is little evidence of slow slip. The 2005 event is imaged to have bilateral rupture with northwestern slip occurring for about 50 s before it moved to the southeast of the epicenter.

Citation: Ishii, M., P. M. Shearer, H. Houston, and J. E. Vidale (2007), Teleseismic *P* wave imaging of the 26 December 2004 Sumatra-Andaman and 28 March 2005 Sumatra earthquake ruptures using the Hi-net array, *J. Geophys. Res.*, *112*, B11307, doi:10.1029/2006JB004700.

1. Introduction

[2] The magnitude and extent of the disastrous 26 December 2004 earthquake remained uncertain for an unusually long time after the event. Reported magnitude changed from 6.2 to 9.0 within a day, but the exact size of the event was still controversial after a few months [e.g., *Lomax*, 2005; *Ni et al.*, 2005; *Stein and Okal*, 2005]. The earthquake was initially thought to have ruptured to an extent of about 300 km northwest of the Sumatra island within about 300 s, but later studies argued that both the extent and duration were much longer [e.g., *Ni et al.*, 2005; *Stein and Okal*, 2005]. The difficulty in determining the characteristics of this earthquake arises from its unusual size, and there have been a number of approaches proposed for studying such monstrous earthquakes [e.g., *Ishii et al.*, 2005; *Krüger and Ohrnberger*, 2005a; *Lomax*, 2005; *Menke and Levin*, 2005; *Ni et al.*, 2005; *Ammon et al.*, 2006; *Blewitt et al.*, 2006; *Larmat et al.*, 2006; *Lockwood and Kanamori*, 2006]. Here we investigate the back-projection technique employed by *Ishii et al.* [2005] and *Walker et al.* [2005], which is an extension of previous ideas [e.g., *Spudich and Cranswick*, 1984; *Ellsworth*, 1992] and works well even for events of large size and long duration.

[3] Conventional methods for studying earthquakes involve calculation of the Green's function to match the computed synthetic seismograms with ground-motion data [e.g., *Hartzell and Helmberger*, 1982; *Olson and Apsel*, 1982; *Cohee and Beroza*, 1994; *Cotton and Campillo*, 1995; *Zeng and Anderson*, 1996; *Sekiguchi et al.*, 1996; *Ji et al.*, 2002; *Frankel*, 2004] and to match computed displacements with geodetic information [e.g., *Hartzell and Heaton*, 1983; *Wald et al.*, 1991; *Yoshida et al.*, 1996; *Song et al.*, 2005]. These models provide the detailed spatial distribution of slip amplitude, rupture speed, and source-time function, and have shown that, for example, slip on a

[1]Department of Earth and Planetary Sciences, Harvard University, Cambridge, Massachusetts, USA.
[2]Institute of Geophysics and Planetary Physics, Scripps Institution of Oceanography, University of California, San Diego, La Jolla, California, USA.
[3]Department of Earth and Space Sciences, University of Washington, Seattle, Washington, USA.

0148-0227/07/2006JB004700$09.00

fault can be highly variable. The back-projection technique presented here complements the Green's function approach.

[4] There are a suite of methods that take advantage of the time-reversal property of the wave equation to identify various sources of seismic energy [e.g., *McMechan et al.*, 1985; *Reitbrock and Scherbaum*, 1994; *Ekström et al.*, 2003; *Kao and Shan*, 2004, 2007; *Baker et al.*, 2005; *MacAyeal et al.*, 2006]. The back-projection technique is one such method, and its advantage resides in the simplicity (hence real-time applicability) of the calculations. For example, it does not require extensive computation of the wavefield even when the three-dimensional structure of the Earth is considered, nor does it require a priori knowledge of the duration and geometry of the event. Another advantage of the back-projection method is that it can be applied easily to data at almost any frequency, including frequencies above 1 Hz. These high frequencies have important implications for structural engineering studies and are sensitive to dynamics of earthquakes, such as acceleration of rupture and rapid changes in slip amplitude [e.g., *Das and Aki*, 1977; *Madariaga*, 1977].

[5] In this paper, we present detailed methodology of the back-projection analysis [*Ishii et al.*, 2005] and explore ways to correct for wavefront distortion due to three-dimensional wave-speed variations. The properties of the 2004 Sumatra-Andaman as well as the 28 March 2005 Sumatran (Nias) earthquakes are investigated with the back-projection technique using the short-period raw data from the Hi-net array in Japan. We also address the spatial and temporal resolution of the models obtained from the back-projection analysis and discuss implications for estimates of characteristics such as the propagation speed.

2. Theory

[6] A wavefront arriving at an array of stations provides information about the source of the energy through its amplitude, curvature, and incident angle [e.g., *Spudich and Cranswick*, 1984; *Goldstein and Archuleta*, 1991; *Ellsworth*, 1992]. This implies that the complexities of the wavetrain can be back-projected and stacked at a grid of potential source locations to unravel the source properties. Mathematically, the stack $s_i(t)$ at the ith potential source grid point as a function of time t can be expressed as a sum over n seismograms, i.e.,

$$s_i(t) = \sum_{k=1}^{n} \alpha_k \, u_k\left(t - t_{ik}^{p}\right),$$

where α_k is the weighting factor for each seismogram, $u_k(t)$ is the seismogram at the kth station, and t_{ik}^{p} is the predicted travel time between the grid point i and station k calculated using a one-dimensional Earth model (e.g., PREM) [*Dziewoński and Anderson*, 1981]. The predicted time shift t_{ik}^{p} represents the changes in the wavefront curvature and incident angle with source location. It leads to a coherent, high-amplitude stack if the position i is indeed the energy source. Each stack $s_i(t)$ estimates time-dependent seismic energy release at the location i, and by combining $s_i(t)$ from all grid points, one can obtain an estimate of spatial and temporal variations in seismic radiation for the event.

[7] For real data, the wavefront is distorted by lateral variations in wave speed within the Earth. We can counter this effect and enhance the coherence of stacks by cross-correlating seismograms, assuming that the waveforms are similar among stations and that they are well-recorded with high signal-to-noise ratio to warrant cross correlation. The perturbations in time obtained from waveform cross correlation, however, introduce an uncertainty in the hypocentral location. We fix the location to that determined from other means, such as event information provided by the USGS National Earthquake Information Center (http://earthquake.usgs.gov/regional/neic/). The stacks then take the form of

$$s_i(t) = \sum_{k=1}^{n} \alpha_k \, u_k\left(t - t_{ik}^{p} + \Delta t_k\right), \tag{1}$$

where Δt_k is the time shift obtained from cross correlation, and represents effects due to heterogeneous wave speed and station-specific corrections such as time calibration error. Note that because each individual seismogram is normalized by α_k, the stacks cannot be directly interpreted in terms of physical parameters such as energy. However, they can provide estimates of the strength of relative seismic energy release within the frequency band of our data, and we will use the term "energy release" in reference to this measure.

[8] The cross-correlation procedure also provides relative amplitude and polarity information of each seismogram with respect to a reference stack. The polarity p_k is used to ensure correct polarity, and the amplitude factor A_k is used to normalize each seismogram. With these two parameters, the weighting value α_k in equation (1) can be defined as

$$\alpha_k = \frac{p_k}{A_k}.$$

If other forms of weighting w_k are desired, such as a weighting that depends on station location (see Supplementary Material[1]), the weighting factor α_k can be modified to

$$\alpha_k = \frac{p_k}{A_k} \, w_k.$$

In addition to normalizing each seismogram, the process of waveform cross correlation provides an opportunity to control the quality of seismograms used in the calculation of stacks. The correlation coefficient between a seismogram and the reference stack is used to discard those that are noisy or have significant waveform distortion.

2.1. Time Calibration

[9] The time correction Δt_k obtained from cross correlation of the initial few seconds of a wavetrain mainly represents variations in travel time due to lateral variations in wave speed between the hypocenter and the kth station. This is insufficient for large earthquakes for which the rupture may extend to areas far away from the hypocenter, or when there are significant small-scale wave-speed variations. Ideally, we would like a time correction for each grid-

[1] Auxiliary materials are available in the HTML. doi:10.1029/2006JB004700.

point-to-station path. We estimate this correction empirically using aftershocks.

[10] Aftershocks are generally distributed near or on the mainshock slip plane, and the cross-correlation of the aftershock waveforms generates time shifts for each aftershock-station location pair. For each station, these time shifts are interpolated or extrapolated to evaluate time shifts at each grid point. Because the distribution of aftershocks is not uniform, the correction at each grid point is determined by an average of aftershock time shifts weighted according to the distance between each aftershock and grid location, and the quality of the records. For each grid point i and station k, the time shift Δt_{ik} is calculated as

$$\Delta t_{ik} = \left(\sum_{j=1}^{m} \frac{\omega_j \Delta t_{jk}}{\Delta_{ij}} \right) / \left(\sum_{j=1}^{m} \frac{\omega_j}{\Delta_{ij}} \right), \quad (2)$$

where Δt_{jk} is the time shift from the j'th aftershock, ω_j is the measure of data quality for the aftershock, and Δ_{ij} is the distance between each aftershock j and grid point i. The summation is over m aftershocks. If the aftershock location coincides with a grid point, the time shift from the event is assigned to the grid point without averaging. The stacks $s_i(t)$ are then calculated with the time shifts, Δt_{ik} at each grid point i and station k, which replaces Δt_k in equation (1), i.e.,

$$s_i(t) = \sum_{k=1}^{n} \alpha_k \; u_k\left(t - t_{ik}^{p} + \Delta t_{ik}\right).$$

2.2. Modeling Specifics

[11] The theory presented in the preceding sections can be applied to any one or a combination of seismic phase arrivals or source-grid geometries. In this study, we use the first-arriving P waves because they are relatively easy to cross-correlate and also because obtaining good source characterization with this phase would be useful in hazard mitigation. Furthermore, we assume the rupture lies on a horizontal plane, i.e., the source grid is two-dimensional with the depth fixed to the hypocentral depth. The P-wave arrival times have poor sensitivity to source depth, and consequently, the resolution of the rupture in the vertical direction is lacking. One could prescribe the dip of the source grid to that defined by seismicity or the slab imaged by seismic tomography. However, the slab profile along the Sumatra-Andaman subduction zone shows remarkable variability, and there are differences among the different tomographic models. Noting that the dips of the two earthquakes investigated in this study are small [e.g., *Ammon et al.*, 2005], we use the horizontal-plane assumption.

3. Data

[12] We apply the back-projection technique to the Sumatra-Andaman earthquake of 26 December 2004, and the Sumatran (Nias) earthquake of 28 March 2005. The array data used in this study come from one of the finest arrays in the world, the High Sensitivity Seismographic Network (Hi-net), in Japan. Implementation and operation of this array was motivated by the damaging Kobe (Hyougo-ken Nambu) earthquake in 1995 [*Okada et al.*, 2004], and it has been in operation since October 2000 [*Obara et al.*, 2005]. The network consists of about 700 stations spaced at roughly 20-km intervals throughout Japan (Figure 1). Each station is equipped with a borehole short-period instrument (100 samples/second, usually three components) that is typically about 100 m below the surface. The depth of the instrument installation suppresses surface noise, resulting in high-quality seismograms.

[13] With respect to the 2004 Sumatra-Andaman event, the array is located at approximately 51° epicentral distance and 43° azimuth. The location with respect to the March 2005 event is similar, with 51° epicentral distance and 42° azimuth. These distances are suitable for teleseismic P-wave analysis, and the thrust mechanisms of the two earthquakes are such that the P waves are well-recorded by the Hi-net stations. We focus on the P waves in this study, hence only the vertical component is used. In addition, because one of the aims of the back-projection technique is the assessment of event properties in near real-time, raw, unfiltered data are used.

[14] Figures 2a and 2b show examples of raw P waveforms from the 2004 Sumatra-Andaman and 2005 Sumatran earthquakes. As noted by other investigators [e.g., *Ni et al.*, 2005], the waveform of the 2004 event is considerably more complex and lasts for a longer time than that of the 2005 Sumatran earthquake. Even though relatively high-frequency recordings are expected to suffer from waveform distortion due to small-scale heterogeneities beneath stations, the initial few seconds of the teleseismic P waveforms are similar among stations throughout the array. This coherence ensures successful retrieval of time shift, relative amplitude, and polarity information through cross correlation and is essential for effective application of the back-projection technique.

[15] The waveform cross correlation is performed on a 4-s window around the expected arrival time as predicted by the one-dimensional model IASP91 [*Kennett and Engdahl*, 1991]. This window is allowed to move by ±2 s. Each seismogram is cross correlated with every other seismogram, and cluster analysis is used to group stations with similar waveforms [e.g., *Romesburg*, 1984]. The cluster tree is cut with a correlation coefficient of 0.6, and seismograms from the largest cluster are stacked to generate a reference stack. This reference stack is correlated against each seismogram, and seismograms having correlation coefficients above 0.6 are stacked to create the next-generation reference stack. This step is repeated five times to obtain a stable reference stack. The time shift Δt_k, amplitude A_k and polarity p_k used in the back-projection procedure (equation (1)) are those resulting from the correlation between each seismogram and the final reference stack. If a seismogram has a correlation coefficient below 0.7, it is not used to calculate the stacks $s_i(t)$. For an event with well-recorded P waves, this selection criterion typically reduces the number of seismograms to about 80% of the ~700 stations available. Some of the waveforms, aligned and selected through the cross-correlation procedure, are shown in Figure 2c.

[16] For time-calibrated back-projection analysis, we choose aftershocks using the signal-to-noise ratio. This ratio is calculated using a 10-s noise window between 5 and 15 s before the P arrival, and a 15-s signal window between −5 and 10 s after the P arrival. The signal-to-noise ratio is calculated for all stations, and earthquakes with the median

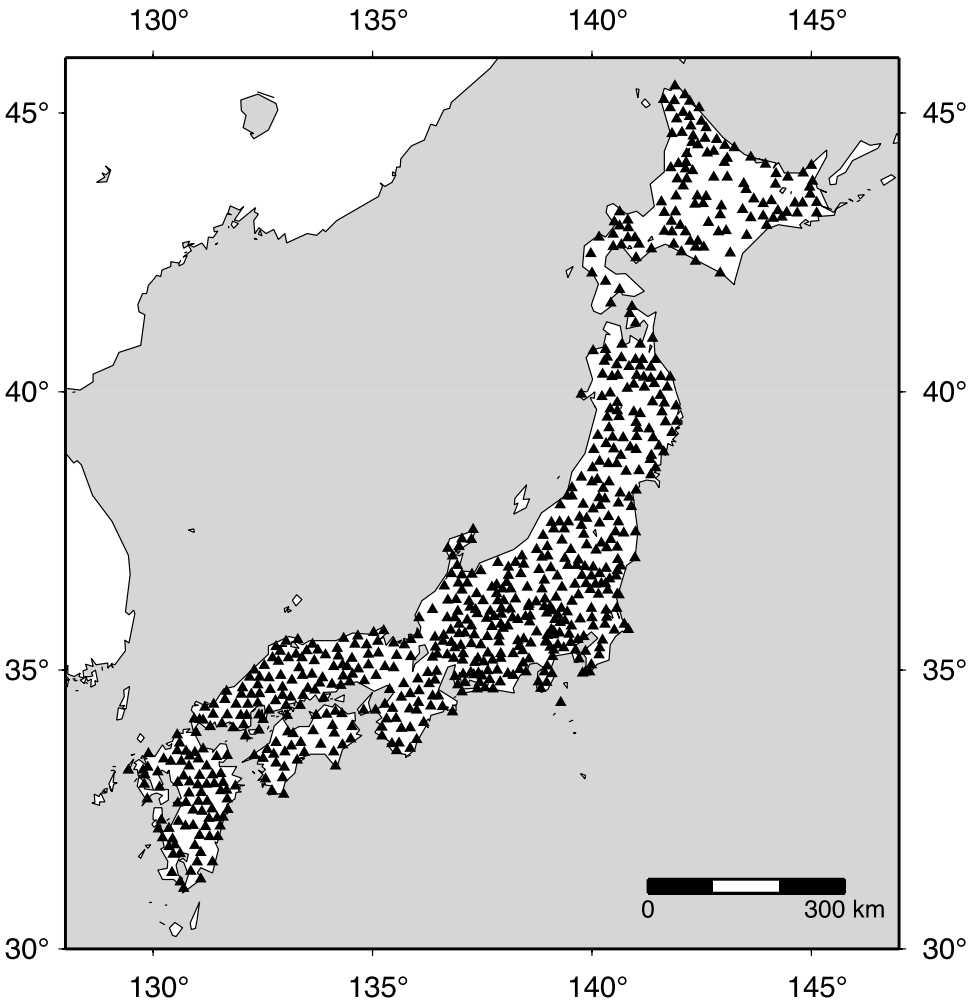

Figure 1. Distribution of about 700 stations (black triangles) throughout Japan that comprise the Hi-net seismic array.

signal-to-noise ratio below 2.0 are removed. The *P*-wave arrivals of the selected aftershocks are cross-correlated to compile a database of time shifts. The expansion of the time shifts is performed as given in equation (2) using the median signal-to-noise ratio as the weighting for individual aftershock ω_j. The smaller size of these aftershocks can potentially mean that there are inaccuracies in hypocentral location and timing. In an attempt to avoid mapping these uncertainties into the time calibration, we remove the average value of the time shifts for each aftershock, i.e., $\Delta t_{jk} = \Delta t^0_{jk} - \Sigma_k \Delta t^0_{jk}/N$, where N is the number of stations, and t^0_{jk} indicates the time shift values obtained from the cross-correlation procedure. This implies that small-scale structure near the source may also be removed, but there is little spatial coherence in the values of the averages, suggesting that they come mainly from uncertainties in source location and timing.

4. Results

4.1. Sumatra-Andaman Earthquake of 26 December 2004

[17] There were 686 Hi-net stations operating at the time of the earthquake. The *P*-wave arrivals from this earthquake are clearly recorded at most stations (Figures 2a and 2c), but the minimum cross correlation criterion reduces the number of seismograms to 546. The time corrections Δt_k are somewhat scattered, ranging from about −4 to 6 s and with an average value of −0.42 s with respect to the predicted arrival time [*Kennett and Engdahl*, 1991]. The source grid for this earthquake covers latitudes between 1.27 and 16.27°N and longitudes between 88.82 and 98.82°E with grid spacing of 0.2° in both latitude and longitude (Figure 3a). The depth of the source grid is fixed at the hypocentral depth of 30 km as determined by the USGS National Earthquake Information Center. Because some of the results using the back-projection method with a single time correction have been presented elsewhere [*Ishii et al.*, 2005], only the results required for comparison with those using distributed time corrections are included in this paper.

4.1.1. Results Using Only the Hypocentral Time Correction

[18] The simplest way to visualize the spatial and temporal variations in energy release given by the stacked seismograms is to generate figures of energy distribution at some time interval [*Ishii et al.*, 2005]. These time slices illustrate that the 2004 Sumatra-Andaman earthquake re-

leased energy unidirectionally for about 550 s, propagating northwestward for about 300 s before changing to a northeastern direction. To grasp the total area and distribution of slip, the stacks are integrated over 600 s (Figure 3b) to obtain an estimate of the relative strength of the total energy release as a function of location. Note that because each seismogram is normalized by the amplitude factor A_k, the back-projection analysis presented here can only give the relative strength of energy release and does not constrain its absolute level. Nonetheless, several observations can be made. The largest amount of *P*-wave energy is released in the southern part of the rupture, a region west of the northern Sumatra Island. There is a second peak occurring at about 300 s after event initiation, which happens west of the Nicobar island chain. The extent of the rupture is about 1300 km, extending from northern Sumatra to the northern part of the Andaman archipelago.

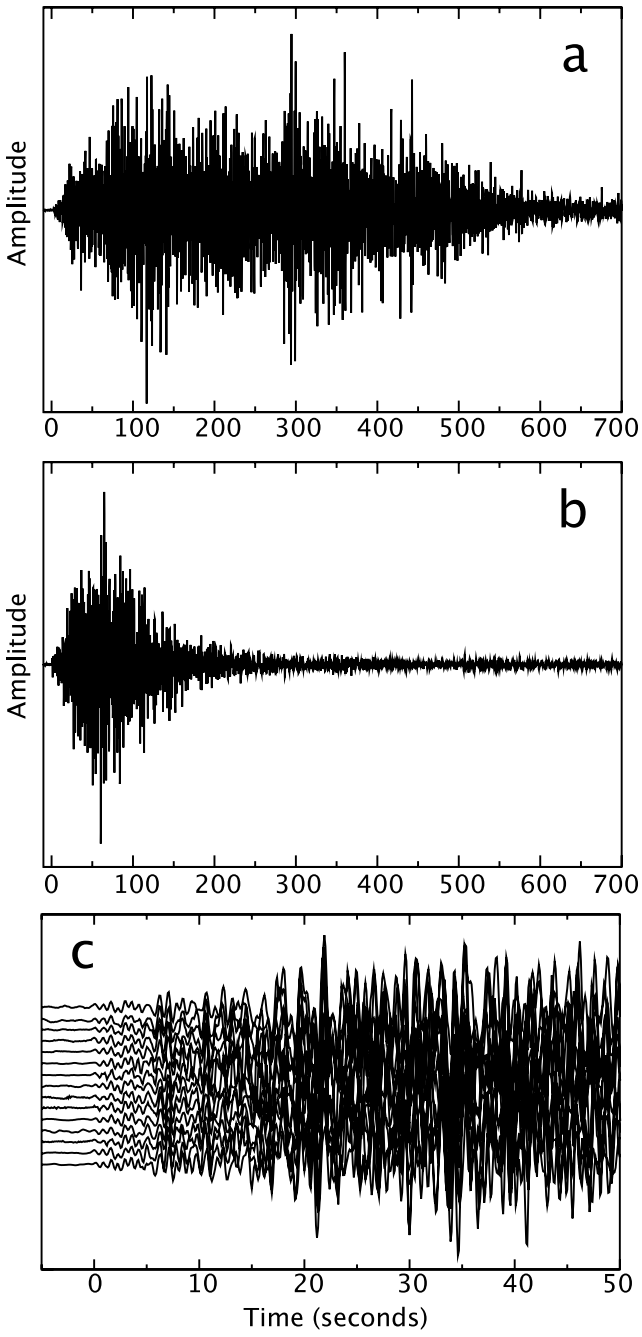

Figure 2. (a) The *P* wavetrain from the 26 December 2004 Sumatra-Andaman earthquake recorded by the station TZWH which is located at 53.7° epicentral distance and 42.6° azimuth from the source. The expected *P* arrival is at time zero and the time series has been decimated to a 5 Hz sampling rate. Note that the *P*-wave arrival lasts for almost 600 s. (b) Same as in Figure 2a except for the 28 March 2005 Sumatran earthquake. The distance and azimuth at the station are 53.8° and 41.4°, respectively. The *P* wavetrain is considerably simpler for this smaller event. (c) Comparison of 15 *P* wavetrains from the 2004 Sumatra-Andaman earthquake plotted using time shift and amplitude information obtained through the cross correlation procedure. The vertical axis is the amplitude of the traces except that the traces have been shifted arbitrarily to allow comparison. Note that the waveforms are very similar in the first 10 s, but the coherency degrades rapidly afterward. This suggests that the source of seismic energy is moving away from the hypocenter.

4.1.2. Results Using Aftershock Time Corrections

[19] For this earthquake, aftershocks occurring between 26 December 2004 and 26 January 2005 at latitudes between 1 and 17°N and longitudes between 88 and 99°E are considered. There are 110 events with depths less than 100 km and magnitudes greater than or equal to 5.0 in the National Earthquake Information Center catalog. When the signal-to-noise selection criterion is applied to these 110 events, the number of earthquakes reduces to 46. The aftershocks used for time calibration are summarized in Supplementary Table 1 and their distribution is shown in Figure 3c by small black stars.

[20] The time-averaged map of energy release obtained with aftershock time calibration is shown in Figure 3c, which differs considerably from the map based upon hypocentral correction (Figure 3b). The latter is spatially very smooth, whereas the former contains significant smaller-scale features. For example, Figure 3c contains blue (low energy release) features around some aftershocks used in the calibration. They are due to time shifts that act to cause destructive interference of waveforms, and result in diminished amplitudes around the aftershock location, demonstrating the increased resolution with the aftershock time calibration. Although these low energy regions are more noticeable, aftershock calibration does not always result in defocusing. For example, time shifts associated with an event at 5.05°N and 92.28°E (occurring on 1 January 2005) constructively stack the mainshock seismograms. Consequently, the region of high energy extends farther to the west toward this aftershock location compared to Figure 3b.

[21] Another significant difference between maps with and without aftershock time calibration is the location and amplitude of the large energy release in the Nicobar-Andaman region. The secondary maximum west of the Nicobar islands in Figure 3b is replaced by a stronger maximum northeast of the Car Nicobar island (Figure 3c). This change results mainly from time shifts obtained from aftershocks

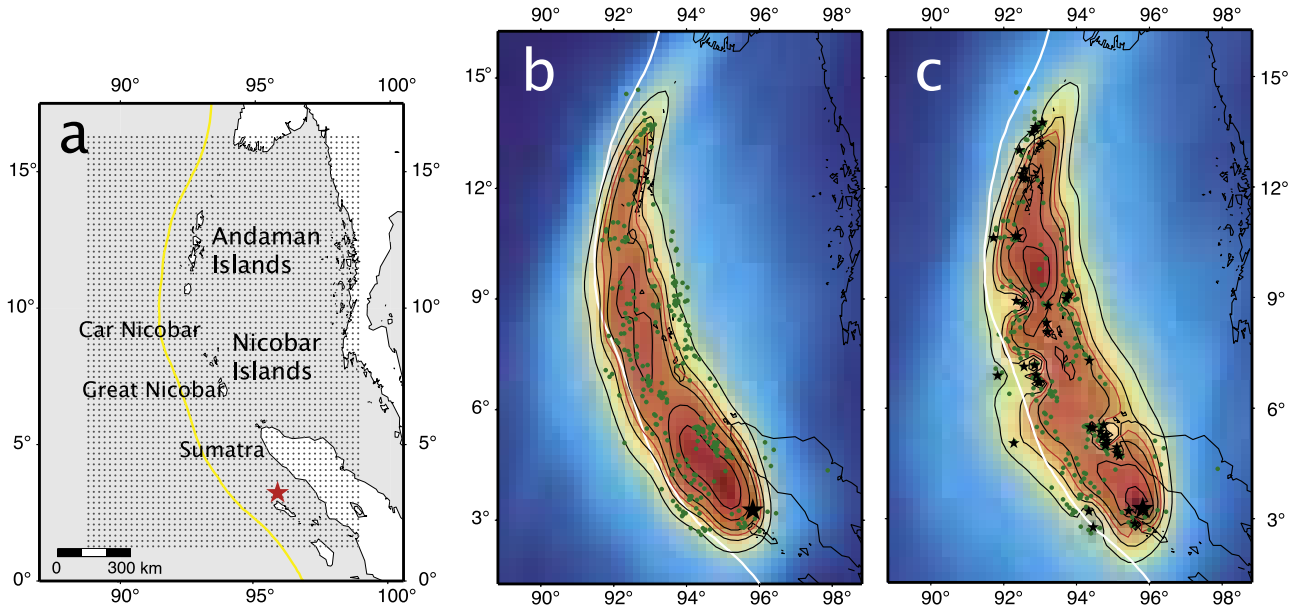

Figure 3. (a) Region of interest around the epicenter. The source grid used for back-projecting the *P* wavetrain for the 26 December 2004 Sumatra-Andaman earthquake is shown by black dots. The depth of this grid is fixed at the hypocentral depth of 30 km. The epicenter is shown by a red star, and names of islands and island chains are given. The plate boundary is shown by the yellow curve. (b) Distribution of relative energy radiation (approximated by the squared amplitude of stacked seismograms) obtained by integrating the first 600 s of the stacked time series with a hypocentral time correction. Warm colors (e.g., red) indicate high levels of energy release and cold colors (e.g., blue) indicate low levels of energy release. The epicenter is indicated by the large black star, and the aftershocks that occurred between 26 December 2004 and 26 January 2005 are shown by green circles. The black contours are plotted at 10% increments, starting at 50% of the maximum amplitude and highlight regions of high energy release. The red contour is at the 65% level, which is used in estimating the total rupture area. The white curve shows the plate boundary. (c) Same as in Figure 3b except for using the time calibration based upon 46 aftershocks (small black stars). See Supplementary Table S1 for the list of aftershocks. There is a significant eastward shift in this map compared to Figure 3b where the depth of the slab increases. However, because the grid is fixed at 30-km depth, this map cannot be taken as evidence for rupture at greater depth.

occurring west of the Great Nicobar island and south-west of the Car Nicobar island. These aftershocks are located near the secondary maximum in Figure 3b and corrections associated with these events prevent coherent stacking of the mainshock seismograms in this region.

[22] Because the aftershock distribution is not uniform across the rupture area, the effect of the aftershock calibration on the image will vary. Strictly speaking, the aftershock time calibrations are only correct locally at each aftershock hypocenter and the accuracy of the time corrections and the quality of the image will degrade as one moves away from the hypocenters. However, back-projection imaging is still possible even at large distances from these calibration points, as evidenced by the image obtained using the mainshock cross-correlation results alone. Our time calibration weighting method provides a continuous set of time shifts that effectively interpolates the times to fill in the gaps between the individual aftershock locations. It should be recognized that this is only an approximation to the true time correction function. Thus details in the Figure 3c image are most reliable when they are closest to an aftershock location and it is possible that some distortions may exist in the image that result from the details of our interpolation scheme. However, our new image should have improved resolution and more accurate relative amplitudes compared to that of *Ishii et al.* [2005] because we use more localized time calibrations throughout the image.

[23] In order to assess the time-dependence of the two models, the locations of maximum energy release are compared as a function of time (Figure 4). This plot is created by calculating the distribution of energy release (approximated as the squared amplitude of the stacks) for every 20 s with an averaging window of 50 s, and determining the centroid location of the area with at least 80% of the maximum energy release. It shows that in addition to changes in the distribution and length scale of the energy release, the aftershock calibration process moves the peak energy sources to the east by about 0.5° (Figure 4a). In contrast, the general timing and progression of energy toward the northwest and then the northeast remain the same. The relative source-time functions also show that the two models are similar with the largest and second largest maxima occurring around 80 and 320 s after the event initiation, respectively. The plot is normalized to the max-

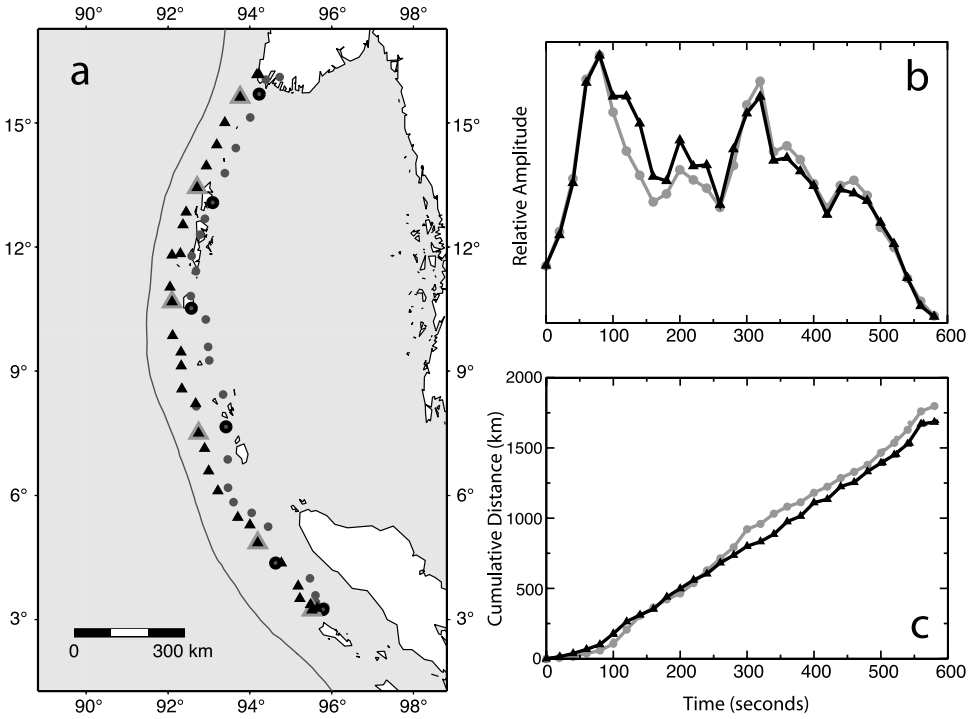

Figure 4. (a) Centroid locations of the amplitude maxima at each time step (20 s) with (grey circles) and without (black triangles) aftershock time calibration. The symbols at every two minutes appear with thick borders to ease visualization of rupture progression between the models. The grey solid curve shows the location of the plate boundary. (b) Comparison of the relative amplitudes between stacks with (grey curve with circles) and without (black curve with triangles) aftershock time calibration as a function of time. These values are taken at locations shown in Figure 4a. (c) Comparison of the cumulative distance as a function of time. This plot is using distance between the two points shown in Figure 4a, but one can alternately calculate cumulative distance along the plate boundary [*Ishii et al.*, 2005] which will give a nearly linear profile with a slope of about 2.8 km/s.

imum value, and shows that the relative energy release at the 320-s maximum is slightly higher for the aftershock-calibrated model. It also differs from the single-calibration model with a relatively lower level of energy release between the two peaks and a slightly higher level after the secondary maximum. The increased level between 300 and 500 seconds is the source of the high amplitude along the Andaman islands observed in the total time-integrated map (Figure 3c). These increases in amplitude occurring in areas far away from the epicenter are expected with aftershock time calibration, because the time corrections become more important as the distance from the hypocenter increases. The aftershock corrections remove the effects of lateral variations more effectively and allow the seismograms to be stacked more coherently.

[24] The propagation speed of the maximum energy release can be calculated using the maximum energy location plot (Figure 4a) by taking the distance between each centroid location and dividing it by the time interval. However, this approach is sensitive to small jumps in location, and gives speeds between 0 to 8 km/s. To avoid these irregularities, cumulative distance is plotted against time for determining the more general trend (Figure 4c). The cumulative distance of the model with no aftershock time calibration smoothly increases with time, and there are two periods with differing slopes: in the first 80 seconds, the slope, i.e., speed, is lower at about 1.3 km/s, but it increases to about 3.1 km/s for the rest of the event duration. The final two data points in Figure 4c occur when the amplitude is close to zero (Figure 4b), and are therefore neglected. In contrast, the slope of the cumulative distance obtained from the aftershock-calibrated model varies considerably. In the first 100 s, it is lower than that with only hypocentral correction, and the slope is about 0.7 km/s. In the following 200 s, it increases to about 3.6 km/s, in comparison to 3.1 km/s for the single time-corrected case. Between 300 and 500 s, the slope becomes gentler, with a speed of about 2.6 km/s. It picks up again between 500 and 560 s to about 4.9 km/s. The robustness of such unusually high speeds is addressed in a later section.

4.2. Sumatran Earthquake of 28 March 2005

[25] The source grid for this earthquake spans latitudes between −1 and 5°N and longitudes between 94 and 100°E with a 0.1° spacing in both directions. The depth of the source grid is set to the hypocentral depth of 30 km as determined by the USGS National Earthquake Information Center. For the aftershock time-calibrated analysis, 58 aftershocks occurring between 28 March and 28 April 2005 within the grid and having depths less than 100 km are considered. Applying the signal-to-noise criterion, the number of events reduces to 23 (see Supplementary Table 2 for a

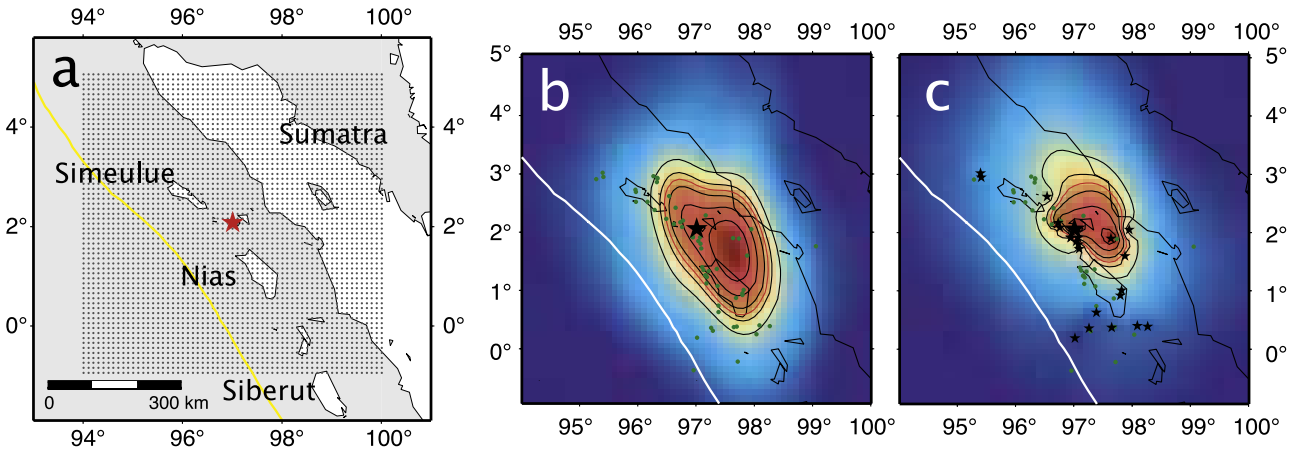

Figure 5. (a) Region of interest around the 28 March 2005 epicenter. The epicenter is shown by a red star, and the source grid at the hypocentral depth of 30 km is shown by black dots. The plate boundary is shown by the yellow curve. (b) Distribution of relative energy release obtained by integrating the first 100 s of the stacked time series with a single time correction using the hypocenter. The epicenter is indicated by the large black star, and the aftershocks that occurred between 28 March and 28 April 2005 are shown by green circles. The black contours start at 50% of the maximum amplitude and indicate high levels of energy radiation at 10% increments. The red contour is at the 65% level, which is used in estimating the total rupture area. The white curve shows the plate boundary. (c) Same as in Figure 5b except for using the time calibration based upon 23 aftershocks (small black stars). See Supplementary Table S2 for the list of aftershocks used in the calculation.

list of events used in the analysis). The distribution of these earthquakes is shown in Figure 5c.

[26] One robust feature observed in results both with and without aftershock time calibration is the bilateral nature (rupture propagation in opposite directions) of the energy release (Figure 6). In contrast to the event of December 2004 for which the rupture propagated in a single direction, the 2005 Sumatran event has energy release northwest of the epicenter in the first 45 to 50 s, followed by energy release southeast of the epicenter. The northwestern extent of the seismic energy release stops short of the area that has been inferred to have slipped during the December event.

[27] The aftershock time calibration results in changes to the images similar to those observed for the 2004 earthquake. For example, the cluster of aftershocks around the epicenter acts to focus seismograms to this area, resulting in high amplitudes that are almost stationary compared to the single correction case where the high amplitude region moves northwest in the first 45 s. An analogous behavior is observed around an aftershock at 97.64°E and 1.9°N.

[28] The relative source time function obtained from the maximum amplitudes, however, is not as sensitive to the time calibration procedure as the distribution of relative energy release. Figure 7a shows that the total duration of the event is about 80 to 90 s. The first 20 s of the earthquake involves low energy release (also recognizable in individual seismograms), followed by a higher, almost steady level of radiation for about 30 s, and the event finishes with its largest energy release in the final 30 s. The constant amplitude period between about 20 and 50 s corresponds to the radiation northwest of the epicenter, and the large energy release after about 50 s corresponds to radiation southeast of the epicenter. When the cumulative distance is plotted, the two regions of activities, one northwest and another southeast of the epicenter, are clearly distinguishable (Figure 7b). The abrupt increase in the cumulative distance at about 50 s occurs when the northwestern rupture terminates and southeastern rupture begins. This transition is not as clear for the aftershock-calibrated model because the northwestern energy release remains close to the epicentral location.

[29] Rupture velocity estimates for the 2005 Sumatran earthquake can be obtained from Figure 7b. Because the amplitude is so small in the first 20 s of the event, the locations of the maximum amplitude points are artifacts of later arrivals with large amplitudes (see Resolvability section) and should be discarded. For the model with only hypocentral correction, fitting a straight line between 20 and 40 s and between 50 and 70 s gives speeds of about 2.5 km/s and 2.7 km/s for the northwest and southeast energy release, respectively. The speeds for the aftershock calibrated model are about 1.0 km/s and 2.8 km/s between 20 and 40 s and between 50 and 70 s, respectively. The lower values for the time-calibrated model in the northwestern rupture results from focusing of energy around aftershocks (Figure 6).

5. Resolvability

[30] In this section, we explore the limitations of the back-projection technique using synthetic seismograms. The synthetic seismograms are represented by a Ricker wavelet with 1-Hz central frequency [*Ricker*, 1953] occurring at the arrival times predicted by the one-dimensional Earth model IASP91 [*Kennett and Engdahl*, 1991]. The location of the energy source is specified in this calculation, and the image recovered from the back-projection of the synthetic seismograms is compared against the input parameters. Note that these synthetic tests are examining the

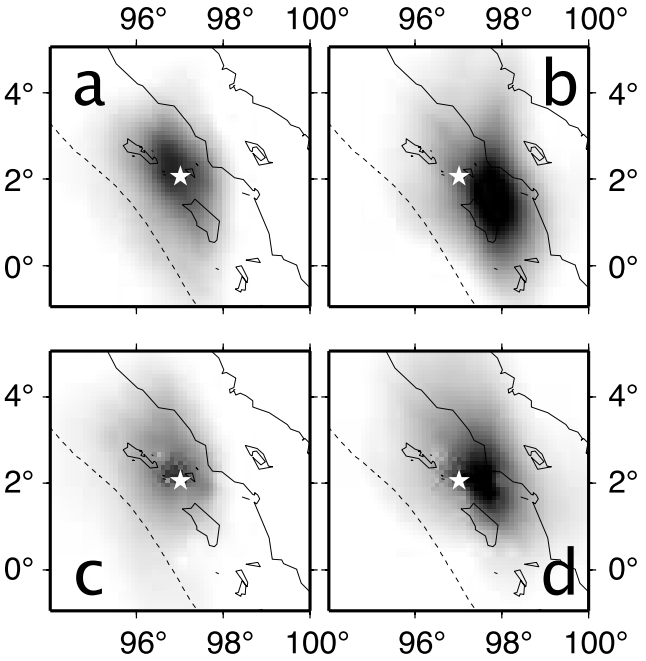

Figure 6. (a) Distribution of the relative energy release (approximated by the square of the stacked seismogram) obtained by integrating the first 50 s of the stacks with only the hypocentral time correction. Dark regions indicate relatively high energy and white regions indicate low energy release. The epicenter is shown by the white star and the dashed line indicates the plate boundary. (b) Same as in Figure 6a except the integration is performed from 50 to 100 s. (c) Same as in Figure 6a except for using stacks with aftershock time corrections. (d) Same as in Figure 6b except for using stacks with aftershock time corrections.

resolution based upon the earthquake location and array geometry for 1-Hz energy radiation. Because we use a one-dimensional model in generating the synthetic seismograms, effects due to incoherent stacking from three-dimensional wave-speed variations are not addressed. Similarly, robustness of results obtained using aftershock calibration cannot be fully addressed using this approach. Nonetheless, the one-dimensional synthetic tests should provide a first-order understanding of the limitations of the back-projection technique due to the geometry of the earthquake and stations and the signal frequency content. For example, these results show the spatial and temporal separation required in resolving two sources.

5.1. Spatial Resolution

[31] We first investigate the spatial resolution of the images obtained through back-projection for the 2004 Sumatra-Andaman earthquake. In this exercise, we focus on the effects of source location and array geometry, hence the synthetic seismograms contain only the *P* waves. Other phases such as *pP* and *PP* are neglected here, but their influence is investigated in the next section. The synthetic input consists of 5 nearly evenly spaced impulsive point sources along the plate boundary (Figure 8a). These sources are offset in time by 100 s from south to north with the first and southernmost source at time zero (Figure 8b). Random noise is added to the synthetic seismograms with signal-to-noise ratio of 20. This value corresponds to the average ratio of the actual recordings used in rupture modeling using −5 to 10 s around the expected *P* arrival time as the signal and 5 to 15 s before the expected arrival time as the noise window. Note that this signal window contains energy arrivals that are small compared to the rest of the *P* wavetrain (Figure 2); hence the synthetics are generated with relatively high noise.

[32] Results of the back-projection analysis using this set of synthetic seismograms determine how a point source broadens due to factors such as limitations in coverage and array geometry. The recovered sources are, in general, elongated in the northeast-southwest direction (Figure 8a). The ellipses are typically about 60 km by 170 km in size, but their shape changes slightly with location. The area of the ellipses increases and the recovered amplitude decreases with increasing latitude, that is, the resolution deteriorates as the rupture propagates northward. The elongation itself is a

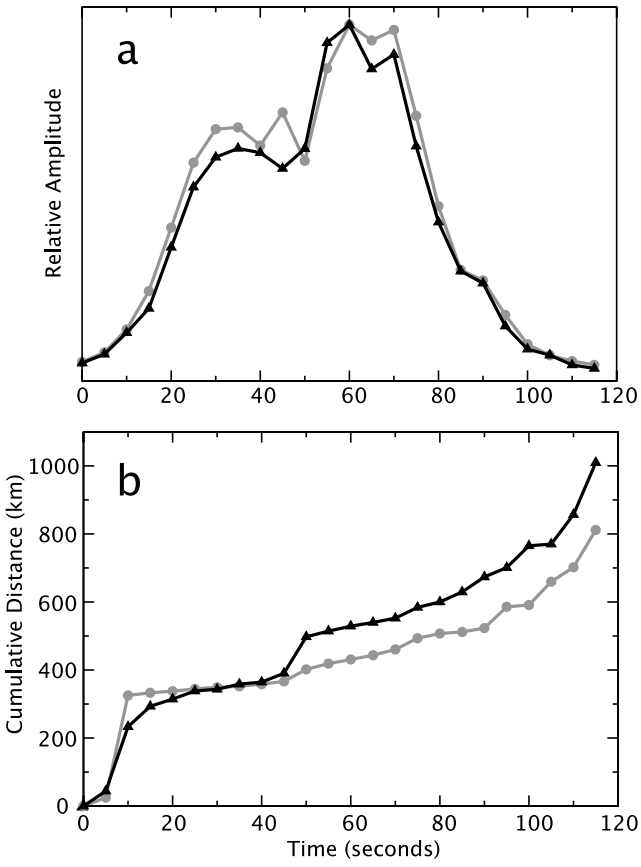

Figure 7. (a) Relative amplitude for the 2005 Sumatran earthquake as a function of time calculated using stacks at 5-s intervals and 20-s integration windows. The black line with black triangles corresponds to the result using a single time correction at the hypocenter, and the grey line with grey circles corresponds to the result using aftershock time corrections. (b) Cumulative distance following the centroid positions of the region with at least 80% of the maximum energy release. Symbols are same as in Figure 7a.

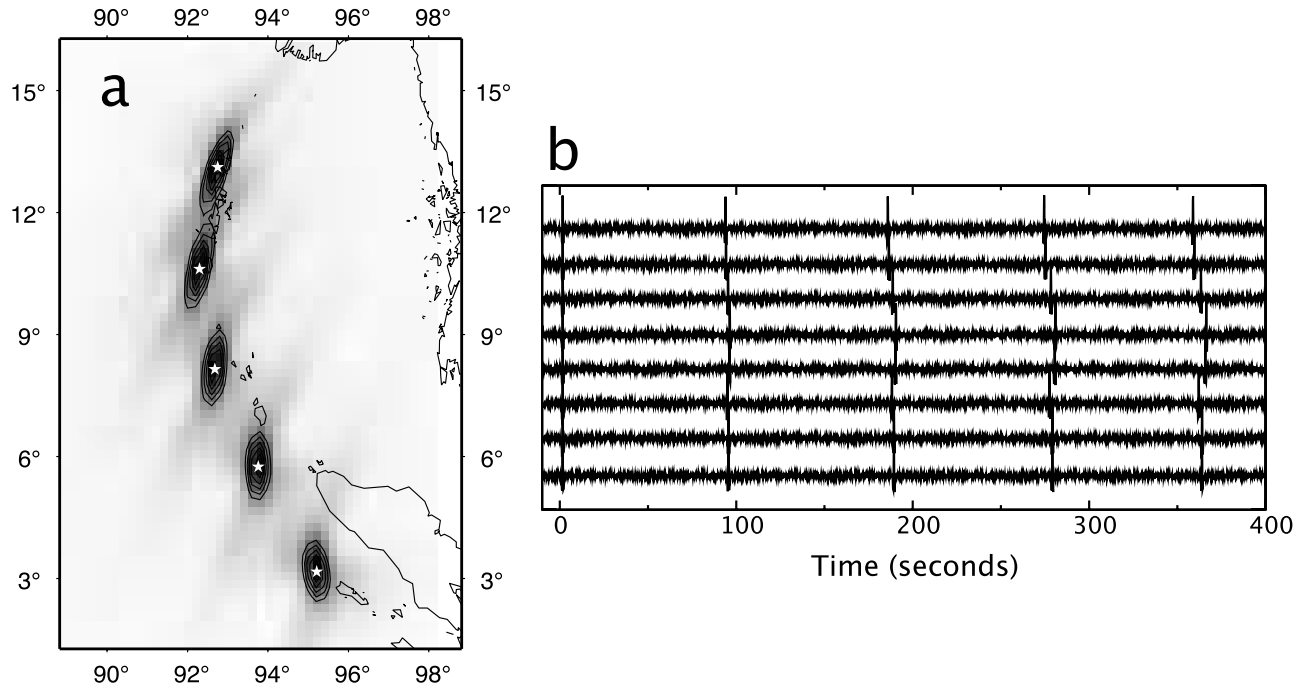

Figure 8. (a) Spatial resolution at five locations along the Sunda arc, corresponding to parts of the rupture plane of the 2004 Sumatra-Andaman earthquake. The input source locations are shown by white stars. The contours are plotted at 10% intervals above 50%. (b) Examples of synthetic seismograms assigned to stations at different distances used to generate Figure 8a. The signal-to-noise ratio is 20 which is the average signal-to-noise ratio for the first 10 s of the 2004 Sumatra-Andaman records. The seismograms have been aligned on the first-arriving pulse from the southernmost source. Only *P* waves are considered, and other phases such as *pP* and *PP* are not included.

result of the array geometry: the Hi-net array is almost linear (Figure 1), and this maps into the source image. On the basis of some experiments, the direction of elongation appears to depend on the location and geometry of the array with respect to the source.

[33] To reduce the elongation effect, one could apply weighting based upon station location and mimic a circular array, suppressing a part of the array geometry effect. This results in source broadening that is more circular (see Supplementary Material). However, because the effective number of stations decreases with the application of such weighting, the resolution becomes poorer (i.e., the area of source broadening increases) compared to results without station weighting. General features obtained from back-projection are unchanged with or without station weighting. Therefore the results with station location weighting are not included in the main text.

[34] The same resolution analysis is performed using a single point source at the hypocenter of the 28 March 2005 Sumatran earthquake with signal-to-noise ratio of 25. At this location, the elongation occurs in the north-south direction (Figure 9). The resolution image is also more circular than those obtained along the 2004 Sumatra-Andaman rupture zone and has dimensions of about 60 km by 135 km. The size is smaller than the total area of rupture in the northwest or southeast of the epicenter (Figure 6) and suggests that the back-projection method using the Hi-net data should be able to detect concurrent slip in the northwest and southeast if it exists.

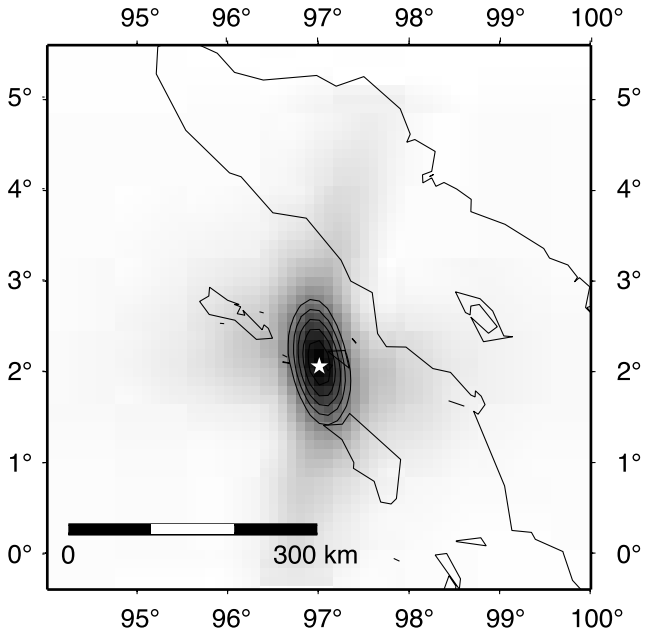

Figure 9. Recovery and broadening of a point source (red star) at the hypocentral location of the 2005 event through synthetic seismograms with only the *P* wave arrivals with signal-to-noise ratio of 25.

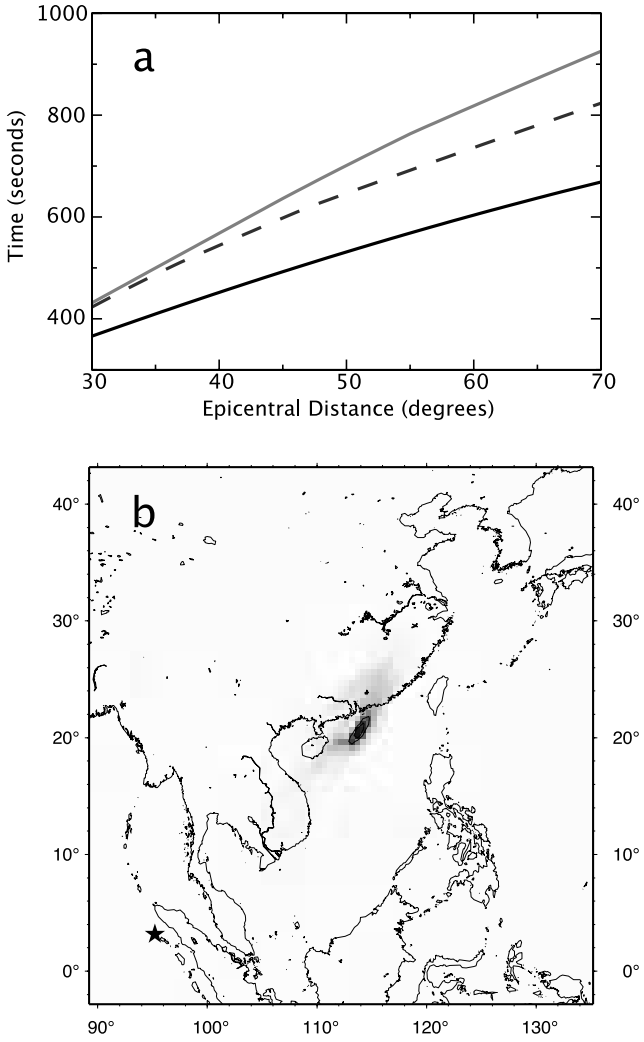

Figure 10. (a) The predicted arrival times of *P* (black solid curve), *PP* (black dashed curve), and *PPP* (grey solid curve) phases between 30 and 70° epicentral distance. Note that the slope (i.e., slowness) of these phases are considerably different. (b) Result of back-projecting the synthetic seismogram consisting only of *PP* arrivals and using the predicted *P* arrival times. The location of the coherent energy stack occurs almost midway between the source (black star) and stations in Japan, around 113°E and 21°N.

5.1.1. Effects of Multiple *P* Arrivals

[35] A complication in earthquake source modeling arises when the earthquake duration is so long that the multiply reflected *P* waves (e.g., *PP* and *PPP*) arrive within the *P* wavetrain. For example, at an epicentral distance of about 60°, the *PP* and *PPP* phases arrive roughly 200 and 300 s after the *P* arrival. The 26 December 2004 Sumatra-Andaman earthquake lasts for more than 500 s, and consequently, the *PP* and *PPP* phases are expected to be present in the window of seismograms used in the back-projection. In this section, we address the possibility of mismapping the energy of these multiply reflected phases into the rupture history.

[36] There are two factors that work in favor of relatively high-frequency back-projection analysis. First, direct *P* is much higher in amplitude than *PP* and *PPP* at frequencies near 1 Hz. Because the multiply reflected waves pass through highly attenuating upper mantle at least two times more than the *P* wave, these waves have lost much of their high-frequency content. Therefore their amplitudes are small at frequencies optimally recorded by the Hi-net array [e.g., *Ni et al.*, 2005]. Second, the slowness of the *P* wave is substantially different from that of the *PP* or *PPP* wave (Figure 10a). This implies that when the stacks are made using the predicted *P* arrival times through t_{ik}^{p} in equation (1), the *PP* or *PPP* waveforms will not stack coherently near the source location. We show this effect in Figure 10b with synthetic seismograms consisting only of *PP* arrivals (c.f. Figure 8b). The *PP* energy back-projects to a point almost midway between the source and the Hi-net array at about 113°E longitude and 21°N latitude. This is because the *PP* slowness is almost twice that of the *P* phase (Figure 10a). Thus the back-projection method applied to the Hi-net data includes inherent frequency and slowness filters that minimize interference from phases other than those assumed in the analysis. This also holds true for other phases such as *S* and *PcP*.

[37] In contrast, the effects of the depth phases (i.e., *pP* and *sP*) are less distinctive. Because the events considered in this study are shallow, the depth phases *pP* and *sP* arrive within a few seconds of the direct *P* arrival. We have performed resolution tests for *pP* and *sP* using a similar approach to those presented for the *PP* phase. These phases back-project to times and locations nearly identical to the source time and location, falling within the spatial and temporal limits of the method and data, as discussed in the previous and next subsections. Indeed, when the synthetic seismogram includes all three phases, *P*, *pP*, and *sP*, the recovered image is nearly identical to that obtained from with only the *P* phase.

5.2. Temporal Resolution

[38] Just as synthetic seismograms from a point source map back into a finite region by imperfect coverage, an impulsive source acquires finite duration. To illustrate this effect and the consequence of integration over a time window used for generating time slices, we analyze a set of synthetic seismograms from an earthquake located at 11.8°N and 92.1°E (Figure 11a). These seismograms include only the *P*-wave arrivals, and the stacks are processed in the same manner as performed for the 2004 Sumatra-Andaman earthquake, i.e., maps of amplitude distribution are calculated at 20-s intervals with a 50-s integration window. We note that in studying smaller earthquakes, it is often better to use smaller increments with less averaging.

[39] The locations of the maximum amplitudes are shown in Figure 11a at 20-s intervals. Because the stations are located within limited ranges of distance and azimuth, destructive interference of waves is not perfect, and stacks are nonzero at times before and after the actual event time. The nonzero energy before the event is located farther away from the array than the epicenter, and this energy moves in the approximate direction of the array. Such a temporal artifact is observed in results using observed seismograms when the amplitude within a wavetrain is highly variable. For example, the weak arrivals at the beginning of the

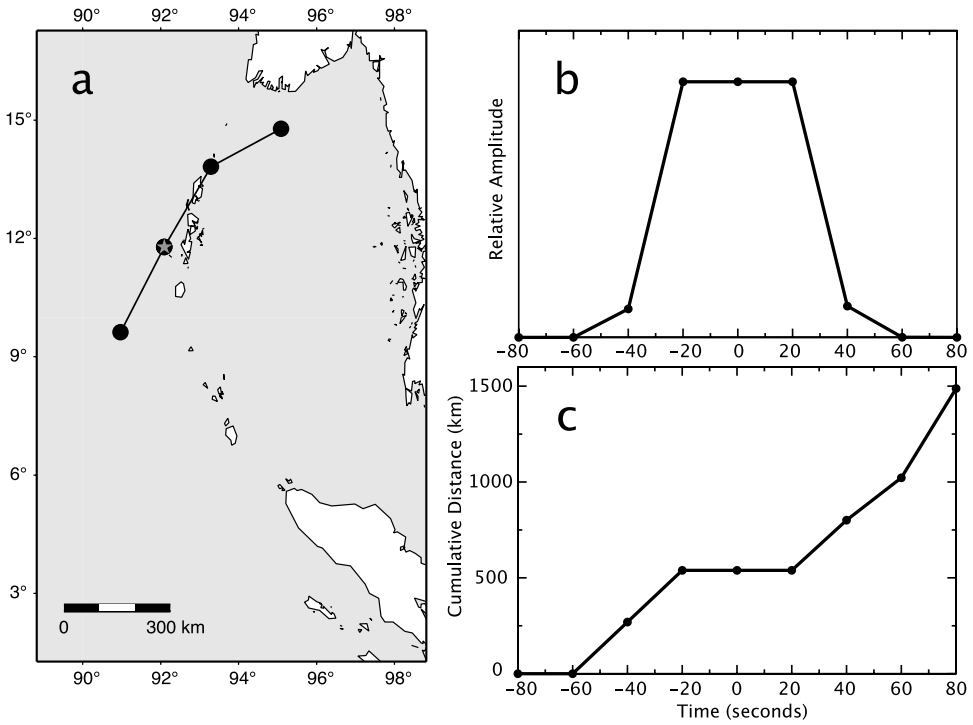

Figure 11. (a) Locations of the maximum amplitude (black circles with black curves) at each 20-s interval between 60 s before and after the occurrence of the synthetic impulsive source (grey star). The left bottom circle corresponds to 60 s before and the top right circle corresponds to 60 s after the event. There are three circles at the epicenter, corresponding to 20 s before and after, as well as the input time. The maximum amplitudes are calculated using a 50-s integration window as used for the 2004 Sumatra-Andaman analysis. (b) Variations in the maximum relative amplitude during the time window shown in Figure 11a. (c) Cumulative distance during the time window shown in Figure 11a.

seismograms of the 2005 Sumatran event are obscured by artifacts of later arrivals with significantly larger amplitudes.

[40] The values of the maximum amplitude obtained from the synthetic test show an increase with time at the beginning, and peaks between 20 s before and after the input time (Figure 11b). During the time when the amplitude is at its peak, the location remains at the epicenter. This behavior around the event time is related to the length of the integration time window. For example, if the integration is performed over 20 s instead of 50 s, the amplitude plateau disappears and is replaced by a more gradual increase/decrease toward/from the epicentral time. Clearly, the artifacts in time and location have significant implications for the calculation of the rupture propagation speed. Plotting the cumulative distance and fitting a straight line to points between -60 and 60 s around the epicentral time gives a slope of about 8.9 km/s (Figure 11c). It is an underestimate, since it averages over the period between -20 and 20 s when the source remains at the epicenter. If this period is ignored, the speed can be as high as about 15 km/s which is close to the apparent speed of *P* waves at 50 degrees distance.

[41] The results of these synthetic tests in time imply that the parameter most affected by artifacts is the estimated propagation speed. If there is strong variation in amplitude within the waveform, the speed estimates can be biased by the movement of the ghost stacks of the high-amplitude part of the seismogram. For example, the initial 20 s and final 10 s of the 90-s long 2005 Sumatran earthquake have energy moving toward the array, and therefore the inferred speeds in these time periods (above 5 km/s) are most likely to be artifacts. Similarly, because the strike of the Andaman islands is similar to the elongation direction of the resolution ellipse, it is possible that the energy propagation speed inferred in this region is overestimated. In contrast, when the rupture is moving nearly perpendicular to the smearing direction such as along the Nicobar islands, the estimates of speed should suffer little from the high speeds associated with the incomplete destructive interference of waveforms.

6. Discussion

[42] The results for the Sumatra-Andaman earthquake of 2004 are, in most part, consistent with other seismically constrained models of the event [e.g., *Ammon et al.*, 2005, 2006; *Krüger and Ohrnberger*, 2005a, 2005b; *Ni et al.*, 2005; *Stein and Okal*, 2005; *Tsai et al.*, 2005]. In all seismic models, the largest release of energy occurs northwest of the Sumatra island where no significant slip has been observed for at least 200 a [*Bilham et al.*, 2005]. Slip inversion models also reveal a low slip area west of the Great Nicobar island [e.g., *Ammon et al.*, 2005; *Vigny et al.*, 2005], similar to low amplitude regions observed in the time-calibrated back-projection result. The second large energy release in

the northern part, near Car Nicobar island and release along the Andaman islands are subdued or not present in early seismically inferred models. The longer-period source studies with body waves must battle the noise from *PP* and *PPP* at times when slip along the northern islands is observed. On the other hand, the high amplitude in this area is consistent with relatively large slip obtained from inversions of geodetic data [e.g., *Banerjee et al.*, 2005] or inferences made from tide gauge records [e.g., *Neetu et al.*, 2005]. In addition, later seismological models with consideration of the enormous size of the event or improved techniques show relatively large moment release in this region [e.g., *Tsai et al.*, 2005; *Ammon et al.*, 2006].

[43] The incorporation of the aftershock data to better correct for three-dimensional structure within the Earth refines the model of the relative energy release. In the case of the 2004 Sumatra-Andaman earthquake, the slip distribution estimated by the Green's function method is quite heterogeneous [e.g., *Ammon et al.*, 2005]. The back-projection result without aftershock corrections does contain heterogeneities but they are much smoother. On the other hand, the model corrected with aftershocks starts to reproduce smaller-scale features such as no or very small slip slightly northwest of Sumatra where a dense population of aftershocks occur [e.g., *Ammon et al.*, 2005]. The qualitative similarities in the shape of high energy release and slip region along the Nicobar archipelago between the models obtained with the Green's function approach and back-projection with aftershock correction are remarkable [e.g., *Bilham*, 2005]. Comparison of the models along the Andaman island chain is harder, because those based upon finite source modeling show considerable variation between various research groups [e.g., *Ammon et al.*, 2005].

[44] The amplitude distribution in space and time obtained from back-projection of the Hi-net array data (e.g., Figures 4b and 7a) represents the relative amplitude of energy radiated toward Japan within the high-frequency bandwidth of the data. Because this is a relative measure over only part of the focal sphere based upon data that cover only part of the complete source radiation spectrum, it cannot be used directly to estimate the total radiated *P*-wave energy. Even if the radiated energy is proportional to our observations, additional assumptions would be required to estimate moment and slip, because the energy to moment ratio varies among earthquakes [e.g., *Kanamori et al.*, 1993; *Ide and Beroza*, 2001] and presumably can also vary during rupture. In addition, for a large earthquake such as the 2004 Sumatra-Andaman earthquake, the mechanism is likely to change along its 1300 km extent. Therefore the amplitude from the Hi-net data may not be related to the magnitude of slip. For example, in an extreme scenario, the mechanism may change from having the array on the nodal plane to the array being on the maximum on the radiation sphere. The relative amplitude inferred using such an array with a narrow azimuth range increases from zero to a maximum even though the actual energy release of the earthquake may be decreasing.

[45] Another property of the earthquake that has attracted much interest is the rupture speed. Tide gauge modeling of the event favors slow slip in the northern half of the slip region along the Andaman islands [e.g., *Bilham*, 2005], although *Neetu et al.* [2005] pointed out a timing error in one of the critical tide gauges. Some seismological models [e.g., *Ammon et al.*, 2005; *Stein and Okal*, 2005] and models based upon hydroacoustic data [e.g., *de Groot-Hedlin*, 2005; *Guilbert et al.*, 2005; *Tolstoy and Bohnenstiehl*, 2005] have also proposed a reduction in rupture speed for the northern segment. The speed obtained in this paper is the speed at which the maximum short-period energy release propagates. This speed may differ from the rupture speed if the locations of maximum energy release do not coincide with locations of the rupture front, and it may also vary from the rupture velocity measured at much longer period from surface waves. Nonetheless, it is a proxy for rupture speed, and values obtained from back-projection show little change between the southern and northern portions of the 2004 Sumatra-Andaman earthquake. As discussed in the Time Resolution section, the speed along the Andaman islands may be overestimated, so the possibility of lower speeds along the Andaman islands cannot be ruled out. Nevertheless, the presence of strong short-period radiation contradicts reports of a significant slow component to the northern slip [e.g., *Stein and Okal*, 2005]. In contrast to estimates of speed with large uncertainty, the duration of the event is better constrained and is about 9 min. This is in agreement with some seismological studies based upon waveform modeling of body and surface waves that suggest that the 2004 Sumatra-Andaman earthquake lasted for about 9 to 10 min [e.g., *Ammon et al.*, 2005; *Krüger and Ohrnberger*, 2005a, 2005b; *Lay et al.*, 2005; *Tsai et al.*, 2005].

[46] The 28 March 2005 Sumatran earthquake has not been studied as extensively as the 2004 Sumatra-Andaman earthquake, but there are some studies with which the results in this paper can be compared [e.g., *Lay et al.*, 2005; *Walker et al.*, 2005]. The rupture for this earthquake has been consistently inferred to be bilateral with slip in the northwest followed by slip in the southeast as imaged by the Hi-net data. Another robust observation for this event is that the slip does not extend into the region of the 2004 Sumatra-Andaman event. The rupture speed and duration of this event are not well-studied, but the results obtained using the back-projection technique and the Hi-net data are similar to values from other studies [e.g., *Ekström et al.*, 2005; *Walker et al.*, 2005].

[47] Perhaps the most unsatisfying part of the results presented in this paper is the fixed depth of the source grid, forcing the slip to lie on a horizontal plane. This is a reasonable first-order approximation for the two Sumatran earthquakes with subhorizontal rupture, but will be an issue for other earthquakes. Some depth variation is expected even for the Sumatran earthquakes. For example, the eastward shift in back-projection results using aftershock calibration for the 2004 event may be interpreted as rupture occurring at greater depths. However, this cannot be confirmed or negated unless the source grid includes variations in depth. Data can be easily back-projected to a three-dimensional source grid, but obtaining good resolution in the vertical direction will be challenging. Changes in depth produces smaller variations in wavefront curvature and incident angle across a teleseismic array than those produced by changes in horizontal location, making smearing in depth unavoidable.

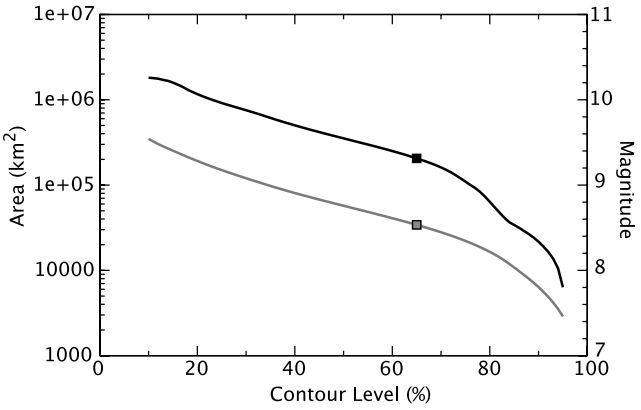

Figure 12. A plot of the total slip area (left axis) or estimated magnitude (right axis) as a function of the cutoff amplitude level between 10 and 95% of the maximum. The result for the 2004 Sumatra-Andaman earthquake is shown in black and that for the 2005 Sumatran event is shown in grey. The squares mark the 65% level used in text. The estimates of area are made using results with hypocentral time correction only.

6.1. Total Slip Area and Moment Magnitude Estimates

[48] Conventional methods used for real-time earthquake monitoring and hazard mitigation are not designed for analysis of unusually large earthquakes such as the 2004 Sumatra-Andaman earthquake. The magnitude of the 2004 event was substantially underestimated: the initial estimates by the National Earthquake Information Center and Pacific Tsunami Warning Center were 6.2 and 8.0, respectively. The consequences of these underestimates for tsunami warning are all too obvious. Clearly, there is a need for a real-time or near real-time source-modeling method which can provide reliable magnitude estimates for the largest of earthquakes.

[49] The moment magnitude M_w of large earthquakes is empirically related to the total slip area S (expressed in units of km^2) such that

$$M_w \sim log_{10}S + 4,$$

as derived from equations given by *Kanamori* [1977]. The spatial distribution of the total radiated high-frequency energy as a function of location is obtained by integrating the back-projected stacks over the event duration (e.g., Figures 3 and 5), and we estimate the total area of slip by choosing some contour level. Using the 65% contour level shown in Figures 3b and 5b, the slip area for the 2004 and 2005 earthquakes with hypocentral time corrections are about 210,000 km^2 and 40,000 km^2, respectively, which translate to moment magnitudes of 9.3 and 8.6, respectively. These values are consistent with those of the Harvard CMT solutions [*Dziewoński et al.*, 1981; *Ekström et al.*, 2005; *Tsai et al.*, 2005].

[50] The 65% level was initially chosen for the 2004 earthquake, not because its magnitude estimate agrees with that from other studies but because the energy level decreases smoothly to the background below the 65% level. This threshold level is also chosen to account for the inevitable broadening of the source region as discussed in the Resolvability section. It is somewhat of an arbitrary choice, and dependence of slip area and magnitude on the threshold contour level is shown in Figure 12. The area estimates with aftershock time calibration are 230,000 km^2 and 14,000 km^2 for the 2004 and 2005 events, respectively, giving magnitudes of 9.35 and 8.15. The correction using aftershocks may increase or decrease the area from that of the single-correction model. However, the choice of the level (65% of the maximum value) may not be appropriate for aftershock-corrected results. For example, the distribution of energy for the 2005 event includes significant spatial variations below the 65% threshold level. On the other hand, there are some models based upon GPS and tide gauge data that have rather a broad slip area or have strong energy release at the boundaries of their models [e.g., *Vigny et al.*, 2005; *Fuji and Satake*, 2007], suggesting that the broadening of the rupture area of the 2004 Sumatra-Andaman event with aftershock correction may be a real feature. Also note that the 65% contour of the aftershock-corrected model is consistent with the spatial distribution of aftershocks.

[51] In addition to source broadening, possible changes in the dip of the slip plane can influence the estimate of the total slip area. Throughout this study, we assume that the slip plane for the two earthquakes is horizontal. Harvard multisource centroid moment tensor solutions, however, indicate that the dip of the 2004 Sumatra-Andaman earthquake ranges between 6 and 8 degrees [*Tsai et al.*, 2005] and the centroid moment tensor solution for the 2005 Sumatran earthquake requires a dip of 8 degrees [*Ekström et al.*, 2005]. If the dip is 8 degrees for both events, then the projection of the horizontal slip area to a dipped plane leads to a 1% increase in the total slip area. For these two earthquakes, the dip of the slip plane results in insignificant changes in the total area and moment magnitude, but this effect would be substantial for other events. Also note that if the dip is as shallow as 8 degrees, then the change in depth for a 200 km width such as that obtained for the 2004 event with aftershock correction gives depth variation on the order of 30 km.

[52] Kanamori's empirical relationship between moment magnitude and slip area [*Kanamori*, 1977] allows determination of the minimum magnitude of an earthquake required for imaging the spatial variations in energy release using the back-projection approach and the Hi-net data. For example, the resolution analysis demonstrates that a point source at the hypocenter of the 2004 Sumatra-Andaman earthquake broadens into an area of approximately 5100 km^2 (Figure 8). This implies that the minimum size of the earthquake for detecting rupture propagation or calculating the moment magnitude based upon the slip area is about M_w 7.7 at this location. This is only a crude assessment, since the shape of the source broadening will have a large impact on resolution. For example, if the slip is moving perpendicular to the minor axis of the resolution ellipse, the minimum magnitude becomes about 7.4. In addition, the shape and size of these resolution ellipses depend upon source location (c.f. Figures 8 and 9), so the threshold magnitude varies with the epicentral location. The theoretical resolution is limited both by the frequency content of the data and the aperture of the Hi-net array. A larger array, such as the global seismic network, could achieve higher resolution and resolve the

rupture details of smaller earthquakes, provided suitable station timing corrections could be obtained [e.g., *Walker et al.*, 2005].

7. Summary

[53] We apply the back-projection technique to the vertical-component seismograms of the 2004 Sumatra-Andaman and 2005 Sumatran (Nias) earthquakes recorded by the Japanese Hi-net array. This approach images the energy release as a function of space and time, leading to constraints on earthquake characteristics such as extent, duration, area, speed, and direction. The method relies upon time shifts obtained from waveform cross correlation to remove the effects due to wave speed variations along the path between the hypocenter and each station. This correction should be sufficient for relatively small events where the rupture is confined within a small region around the hypocenter. However, for a large event such as the 2004 Sumatra-Andaman earthquake, wavefront distortion from three-dimensional wave speed variations for paths originating from points away from the hypocenter becomes important. We approximate these effects empirically by cross-correlating the aftershock waveforms using events occurring within one month following the main event. These aftershock time corrections introduce small-scale features in the distribution of the seismic energy release and allow for better resolution in regions far from the epicenter where aftershocks occurred.

[54] Despite the limited range in azimuth and distance available using the Hi-net array, the properties of the 2004 and 2005 events are well-resolved. The timing and spatial distribution of energy release are consistent with results from other studies. The rupture speed (approximated by the propagation speed of the maximum energy release) has relatively large uncertainty, but the duration and relative amplitude of the events are robust. The biggest advantage of the back-projection approach is that this method can be applied soon after event occurrence without much a priori knowledge. Once the seismic wave (*P* wave in this study) arrives at an array, it takes a few minutes on a desktop computer to perform the iterative cross correlation (the duration depends on the number of stations, number of iterations, and the length of the time window), and another couple of minutes to perform the back-projection, the duration of which depends on the number of grid points considered. The only a priori information required is the hypocentral location which is readily available such as that posted by the USGS National Earthquake Information Center. Detailed analysis using aftershock time calibration requires more time as one must wait for these events to happen. However, earthquakes occur within limited regions around the world (e.g., around the Pacific), so it would be possible to assemble a database of time perturbations for various paths and build a time-calibration grid without the occurrence of aftershocks.

[55] **Acknowledgments.** The authors thank the National Research Institute for Earth Science and Disaster Prevention in Japan for making the Hi-net data available. We also thank Kelin Wang, Honn Kao, and an anonymous reviewer for constructive suggestions. Some figures have been generated using the Generic Mapping Tools [*Wessel and Smith*, 1991]. This research was supported in part by grant EAR–0609092 from the National Science Foundation.

References

Ammon, C. J., et al. (2005), Rupture process of the 2004 Sumatra-Andaman earthquake, *Science*, *308*, 1133–1139.

Ammon, C. J., A. A. Velasco, and T. Lay (2006), Rapid estimation of first-order rupture characteristics for large earthquakes using surface waves: 2004 Sumatra-Andaman earhtquake, *Geophys. Res. Lett.*, *33*, L14314, doi:10.1029/2006GL026303.

Baker, T., R. Granat, and R. W. Clayton (2005), Real-time earthquake location using Kirchhoff reconstruction, *Bull. Seismol. Soc. Am.*, *95*, 699–707, doi:101785/0120040123.

Banerjee, P., F. F. Pollitz, and R. Bürgmann (2005), The size and duration of the Sumatra-Andaman earthquake from far-field static offsets, *Science*, *308*, 1769–1772.

Bilham, R. (2005), Viewpoint: A flying start, then a slow slip, *Science*, *308*, 1126–1127.

Bilham, R., R. Engdahl, N. Feldl, and S. P. Satyabala (2005), Partial and complete rupture of the Indo-Andaman plate boundary 1847–2004, *Bull. Seismol. Soc. Am.*, *76*, 299–311.

Blewitt, G., C. Kreemer, W. C. Hammond, H.-P. Plag, S. Stein, and E. Okal (2006), Rapid determination of earthquake magnitude using GPS for tsunami warning systems, *Geophys. Res. Lett.*, *33*, L11309, doi:10.1029/2006GL026145.

Cohee, B. P., and G. C. Beroza (1994), Slip distribution of the 1992 Landers earthquake and its implications for earthquake source mechanics, *Bull. Seismol. Soc. Am.*, *84*, 692–712.

Cotton, F., and M. Campillo (1995), Frequency domain inversion of strong motions: Application to the 1992 Landers earthquake, *J. Geophys. Res.*, *100*, 3961–3975.

Das, S., and K. Aki (1977), Fault plane with barriers: A versatile earthquake model, *J. Geophys. Res.*, *82*, 5658–5670.

de Groot-Hedlin, C. D. (2005), Estimation of the rupture length and velocity of the great Sumatra earthquake of Dec. 26, 2004 using hydroacoustic signals, *Geophys. Res. Lett.*, *32*, L11203, doi:10.1029/2005GL022705.

Dziewoński, A. M., and D. L. Anderson (1981), Preliminary reference Earth model, *Phys. Earth Planet. Int.*, *25*, 297–356.

Dziewoński, A. M., T. A. Chou, and J. H. Woodhouse (1981), Determination of earthquake source parameters from waveform data for studies of global and regional seismicity, *J. Geophys. Res.*, *86*, 2825–2852.

Ekström, G., M. Nettles, and G. Abers (2003), Glacial earthquakes, *Science*, *302*, 622–624.

Ekström, G., A. M. Dziewoński, N. N. Maternovskaya, and M. Nettles (2005), Global seismicity of 2003: Centroid-moment-tensor solutions for 1087 earthquakes, *Phys. Earth Planet. Int.*, *148*, 327–351.

Ellsworth, W. L. (1992), Imaging fault rupture without inversion, *Seismol. Res. Lett.*, *63*, 73.

Frankel, A. (2004), Rupture process of the M 7.9 Denali Fault, Alaska, earthquake: Subevents, directivity, and scaling of high-frequency ground motions, *Bull. Seismol. Soc. Am.*, *94*, 234–255.

Fuji, Y., and K. Satake (2007), Tsunami source of the 2004 Sumatra-Andaman earthquake inferred from tide gauge and satellite data, *Bull. Seismol. Soc. Am.*, *97*, S192–S207.

Goldstein, P., and R. J. Archuleta (1991), Deterministic frequency-wavenumber methods and direct measurements of rupture propagation during earthquakes using a dense array: Data analysis, *J. Geophys. Res.*, *91*, 7326–7342.

Guilbert, J., J. Vergoz, E. Schisselé, A. Roueff, and Y. Cansi (2005), Use of hydroacoustic and seismic arrays to observe rupture propagation and source extennt of the M_w = 9.0 Sumatra earthquake, *Geophys. Res. Lett.*, *32*, L15310, doi:10.1029/2005GL022966.

Hartzell, S. H., and T. H. Heaton (1983), Inversion of strong ground motion and teleseismic waveform data for the fault rupture history of the 1979 Imperial Valley, California, earthquake, *Bull. Seismol. Soc. Am.*, *73*, 1553–1583.

Hartzell, S. H., and D. V. Helmberger (1982), Strong-motion modeling of Imperial Valley earthquake of 1979, *Bull. Seismol. Soc. Am.*, *72*, 571–596.

Ide, S., and G. C. Beroza (2001), Does apparent stress vary with earthquake size?, *Geophys. Res. Lett.*, *28*, 3349–3352.

Ishii, M., P. M. Shearer, H. Houston, and J. E. Vidale (2005), Extent, duration and speed of the 2004 Sumatra-Andaman earthquake imaged by the Hi-net array, *Nature*, *435*, 933–936.

Ji, C., D. J. Wald, and D. V. Helmberger (2002), Source description of the 1999 Hector Mine, California, earthquake, part I: Wavelet domain inversion theory and resolution analysis, *Bull. Seismol. Soc. Am.*, *92*, 1192–1207.

Kanamori, H. (1977), The energy release in great earthquakes, *J. Geophys. Res.*, *82*, 2981–2987.

Kanamori, H., J. Mori, E. Hauksson, T. H. Heaton, L. K. Hutton, and L. Jones (1993), Determination of earthquake energy release and M_L using TERRAscope, *Bull. Seismol. Soc. Am.*, *83*, 330–346.

Kao, H., and S.-J. Shan (2004), The source-scanning algorithm: mapping the distribution of seismic sources in time and space, *Geophys. J. Int.*, *157*, 589–594.

Kao, H., and S.-J. Shan (2007), Rapid identification of earthquake rupture plane using source-scanning algorithm, *Geophys. J. Int.*, *168*(3), 1011–1020.

Kennett, B. L. N., and E. R. Engdahl (1991), Traveltimes for global earthquake location and phase identification, *Geophys. J. Int.*, *105*, 429–465.

Krüger, F., and M. Ohrnberger (2005a), Tracking the rupture of the M_w = 9.3 Sumatra earthquake over 1150 km at teleseismic distance, *Nature*, *435*, 937–939.

Krüger, F., and M. Ohrnberger (2005b), Spatio-temporal source characteristics of the 26 December 2004 Sumatra earthquake as imaged by teleseismic broadband arrays, *Geophys. Res. Lett.*, *32*, L24312, doi:10.1029/2005GL023939.

Larmat, C., J.-P. Montagner, M. Fink, Y. Capdeville, A. Tourin, and E. Clévédé (2006), Time-reversal imaging of seismic sources and application to the great Sumatra eartquake, *Geophys. Res. Lett.*, *33*, L19312, doi:10.1029/2006GL026336.

Lay, T., et al. (2005), The great Sumatra-Andaman earthquake of 26 December 2004, *Science*, *308*, 1127–1133.

Lockwood, O. G., and H. Kanamori (2006), Wavelet analysis of the seismograms of the 2004 Sumatra-Andaman earthquake and its application to tsunami early warning, *Geochem. Geophys. Geosyst.*, *7*, Q09013, doi:10.1029/2006GC001272.

Lomax, A. (2005), Rapid estimation of rupture extent for large earthquakes: Application to the 2004, M9 Sumatra-Andaman mega-thrust, *Geophys. Res. Lett.*, *32*, L10314, doi:10.1029/2005GL022437.

MacAyeal, D. R., et al. (2006), Transoceanic wave propagation links iceberg calving margins of Antarctica with storms in tropics and northern hemisphere, *Geophys. Res. Lett.*, *33*, L17502, doi:10.1029/2006GL027235.

Madariaga, R. (1977), High-frequency radiation from crack (stress drop) models of earthquake faulting, *Geophys. J. R. Astron. Soc.*, *51*, 625–651.

McMechan, G. A., J. H. Luetgert, and W. D. Mooney (1985), Imaging of earthquake sources in Long Valley caldera, California, 1983, *Bull. Seismol. Soc. Am.*, *75*, 1005–1020.

Menke, W., and V. Levin (2005), A strategy to rapidly determine the magnitude of great earthquakes, *Eos Trans. AGU*, *86*, 185–189.

Neetu, S., I. Suresh, R. Shankar, D. Shankar, S. S. C. Shenoi, S. R. Shetye, D. Sundar, and B. Nagarajan (2005), Comment on "The great Sumatra-Andaman earthquake of 26 December 2004," *Science*, *310*, 1431.

Ni, S., H. Kanamori, and D. Helmberger (2005), Seismology: Energy radiation from the Sumatra earthquake, *Nature*, *434*, 582.

Obara, K., K. Kasahara, S. Hori, and Y. Okada (2005), A densely distributed high-sensitivity seismograph network in Japan: Hi-net by National Research Institute for Earth Science and Disaster Prevention, *Rev. Sci. Instrum.*, *76*, 021301.

Okada, Y., K. Kasahara, S. Hori, K. Obara, S. Sekiguchi, H. Fujiwara, and A. Yamamoto (2004), Recent progress of seismic observation networks in Japan: Hi-net, F-net, K-NET and KiK-net, *Earth Planets Space*, *56*, xv–xxviii.

Olson, A. H., and R. J. Apsel (1982), Finite fault and inversion theory with applicati ons to 1979 Imperial Valley earthquake, *Bull. Seismol. Soc.*, *72*, 1969–2001.

Reitbrock, A., and F. Scherbaum (1994), Acoustic imaging of earthquake sources from the Chalfant Valley, 1985, aftershock series, *Geophys. J. Int.*, *119*, 260–268.

Ricker, N. (1953), The form and laws of propagation of seismic wavelets, *Geophysics*, *18*, 10–40.

Romesburg, H. C. (1984), *Cluster Analysis for Researchers*, 334 pp., Lulu Press, Napa, Calif.

Sekiguchi, H., K. Irikura, T. Iwata, Y. Kakehi, and M. Hoshiba (1996), Minute locating of faulting beneath Kobe and the waveform inversion of the source process during the 1995 Hyogo-ken Nanbu, Japan, earthquake using strong ground motion records, *J. Phys. Earth*, *44*, 473–487.

Song, Y. T., C. Ji, L.-L. Fu, V. Zlotnicki, C. K. Shum, Y. Yi, and V. Hjorleifsdottir (2005), The 26 December 2004 tsunami source estimated from satellite radar altimetry and seismic waves, *Geophys. Res. Lett.*, *32*, L20601, doi:10.1029/2005GL023683.

Spudich, P., and E. Cranswick (1984), Direct observation of rupture propagation during the 1979 Imperial Valley earthquake using a short baseline accelerometer array, *Bull. Seismol. Soc. Am.*, *74*, 2083–2114.

Stein, S., and E. A. Okal (2005), Seismology: Speed and size of the Sumatra earthquake, *Nature*, *434*, 581–XXX.

Tolstoy, M., and D. W. R. Bohnenstiehl (2005), Hydroacoustic constraints on the rupture duration, length, and speed of the great Sumatra-Andaman earthquake, *Seismol. Res. Lett.*, *76*, 419–425.

Tsai, V. C., M. Nettles, G. Ekström, and A. M. Dziewoński (2005), Multiple CMT source analysis of the 2004 Sumatra earthquake, *Geophys. Res. Lett.*, *32*, L17304, doi:10.1029/2005GL023813.

Vigny, C., et al. (2005), Insight into the 2004 Sumatra-Andaman earthquake from GPS measurements in southeast Asia, *Nature*, *436*, 201–206.

Wald, D. J., D. V. Helmberger, and T. H. Heaton (1991), Rupture model of the 1989 Loma Prieta earthquake from the inversion of strong-motion and broadband teleseismic data, *Bull. Seismol. Soc. Am.*, *81*, 1540–1572.

Walker, K., M. Ishii, and P. M. Shearer (2005), Rupture details of the 28 March 2005 Sumatra Mw 8.6 earthquake imaged with teleseismic *P* waves, *Geophys. Res. Lett.*, *32*, L24303, doi:10.1029/2005GL024395.

Wessel, P., and W. H. F. Smith (1991), Free software helps map and display data, *Eos Trans. AGU*, *72*, 441.

Yoshida, S., K. Koketsu, B. Shibazaki, T. Sagiya, T. Kato, and Y. Yoshida (1996), Joint inversion of near- and far-field waveforms and geodetic data for the rupture process of the 1995 Kobe earthquake, *J. Phys. Earth*, *44*, 437–454.

Zeng, Y., and J. G. Anderson (1996), A composite source model of the 1994 Northridge earthquake using genetic algorithms, *Bull. Seismol. Soc. Am.*, *86*, S71–S83.

H. Houston and J. E. Vidale, Department of Earth and Space Sciences, University of Washington, 4000 15th Avenue NE, Seattle, WA 98195, USA. (heidi.houston@gmail.com; john.vidale@gmail.com)

M. Ishii, Department of Earth and Planetary Sciences, Harvard University, 20 Oxford Street, Cambridge, MA 02138, USA. (ishii@eps.harvard.edu)

P. M. Shearer, Institute of Geophysics and Planetary Physics, Scripps Institution of Oceanography, University of California, San Diego, IGPP 0225, La Jolla, CA 92093, USA. (pshearer@ucsd.edu)